Combined experimental and modeling studies of microwave activated $CH_4/H_2/Ar$ plasmas for microcrystalline, nanocrystalline, and ultrananocrystalline diamond deposition

James C. Richley,[1] Oliver J. L. Fox,[1] Michael N. R. Ashfold,[1,a)] and Yuri A. Mankelevich[2]
[1]*School of Chemistry, University of Bristol, Bristol, BS8 1TS, United Kingdom*
[2]*Skobel'tsyn Institute of Nuclear Physics, Moscow State University, Leninskie gory, Moscow, 119991 Russia*

(Received 21 December 2010; accepted 10 February 2011; published online 25 March 2011)

A comprehensive study of microwave (MW) activated $CH_4/H_2/Ar$ plasmas used for diamond chemical vapor deposition is reported, focusing particularly on the effects of gross variations in the H_2/Ar ratio in the input gas mixture (from H_2/Ar mole fraction ratios of $>10:1$, through to $\sim 1:99$). Absolute column densities of $C_2(a)$ and $CH(X)$ radicals and of $H(n=2)$ atoms have been determined by cavity ringdown spectroscopy, as functions of height (z) above a substrate and of process conditions (CH_4, H_2, and Ar input mole fractions, total pressure, p, and input microwave power, P). Optical emission spectroscopy has also been used to explore the relative densities of electronically excited H atoms, and CH, C_2, and C_3 radicals, as functions of these same process conditions. These experimental data are complemented by extensive 2D (r, z) modeling of the plasma chemistry, which provides a quantitative rationale for all of the experimental observations. Progressive replacement of H_2 by Ar (at constant p and P) leads to an expanded plasma volume. Under H_2-rich conditions, $>90\%$ of the input MW power is absorbed through rovibrational excitation of H_2. Reducing the H_2 content (as in an Ar-rich plasma) leads to a reduction in the absorbed power density; the plasma necessarily expands in order to accommodate a given input power. The average power density in an Ar-rich plasma is much lower than that in an H_2-rich plasma operating at the same p and P. Progressive replacement of H_2 by Ar is shown also to result in an increased electron temperature, an increased $[H]/[H_2]$ number density ratio, but little change in the maximum gas temperature in the plasma core (which is consistently ~ 3000 K). Given the increased $[H]/[H_2]$ ratio, the fast H-shifting ($C_yH_x + H \leftrightarrow C_yH_{x-1} + H_2$; $y=1-3$) reactions ensure that the core of Ar-rich plasma contains much higher relative abundances of "product" species like C atoms, and C_2, and C_3 radicals. The effects of Ar dilution on the absorbed power dissipation pathways and the various species concentrations just above the growing diamond film are also investigated and discussed. © *2011 American Institute of Physics*. [doi:10.1063/1.3562185]

I. INTRODUCTION

Activated hydrocarbon/H_2 gas mixtures are widely used for the chemical vapor deposition (CVD) of thin films of diamond.[1] Activation is typically achieved using one (or more) hot filaments, or by microwave (MW) plasma enhanced (PE) excitation. The last decade has witnessed major advances in our detailed understanding of the chemistry and composition of such gas mixtures, and the way these vary with spatial location within the reactor and with changes in process conditions.[2,3] Key to these advances have been (i) the development and application of quantitative spectroscopic techniques for diagnosing selected gas phase species in the activated gas mixture and (ii) the complementary development of models that incorporate realistic treatments of the activation (e.g., power absorption and gas heating), and processing (e.g., heat and mass transfer, chemical kinetics, etc.) of the input gas mixture, and of likely gas-surface processes at substrate.

One variable that has engendered much interest is the fraction of rare gas (e.g., argon) in the process gas mixture.[4–9] Small amounts of argon were added to the process gas mixtures used in many early MW-PECVD studies to help initiate and/or stabilize the plasma and/or to enable actinometry measurements.[10,11] The C/H ratio in the process gas mixture can have a profound effect on the morphology of the as-grown diamond: increasing the C/H ratio by, for example, increasing the CH_4 fraction leads to a reduction in average grain size [e.g., from microcrystalline diamond (MCD) to nanocrystalline diamond (NCD)].[12] Gruen and coworkers pioneered an alternative route to increasing the C/H ratio in the process gas mixture – by progressive replacement of H_2 by Ar.[5,6,13] Such substitution can, in extreme cases (e.g., when using gas mixtures comprising $\sim 1\%CH_4/\sim 1\%H_2/\sim 98\%Ar$), result in the formation of so-called ultrananocrystalline diamond (UNCD) films, in which the individual grains have diameters of just a few nanometers.[14,15] Articles and reviews describing properties and potential applications of such films, and their dependence on grain size, are becoming increasingly common.[16–18] Several recent studies have also provided detailed pictures of the plasma chemistry and composition in MW activated CH_4/H_2 gas mixtures containing a few percent Ar,[2] but none yet has attempted to describe the full spectrum of behavior as the Ar fraction is increased,

a)Electronic mail: mike.ashfold@bris.ac.uk. FAX: (117)-9250612.

and gradually comes to dominate, in a self-consistent way. That is the goal of the present paper, which presents experimental and modeling studies of MW activated C/H/Ar plasmas in which the H_2/Ar ratio in the input gas mixture varies from >10:1 to ~1:99. The experimental program involves spatially resolved [i.e., as a function of height (z) above the substrate surface] measurements of C_2 radicals [in the first excited ($a^3\Pi$) electronic state], CH radicals [in the ground ($X^2\Pi$) state] and H atoms [in their first excited ($n=2$) state] by cavity ringdown spectroscopy (CRDS)[19] and by optical emission spectroscopy (OES)[20] studies of electronically excited H atoms and CH, C_2, and C_3 radicals, as functions of process conditions like the gas mixing ratio, total pressure and input microwave power. CRDS is a very sensitive absorption technique that returns the line-integrated absorbance (LIA) associated with a chosen probe transition. Given appropriate knowledge of the spectroscopy of the target species of interest, the measured LIA can be converted to an absolute column density (i.e., along r) in the quantum state probed by the transition. Converting this quantity to a total column density of the target species (or to a local species number density) is challenging, given the inhomogeneous distribution of gas temperatures (T_{gas} ~3000 K in the center of the plasma ball, but only ~300 K at the internal wall of the CVD reactor) and species number densities along the probed column.

Such data can be obtained, however, by judicious intercomparison between experimental measurement and high level reactor modeling — as illustrated in our previous diagnoses of the gas phase environment in a dc arc jet reactor,[21,22] and in MW activated C/H,[23] B/H,[24] and B/C/H (Ref. 25) plasmas. The companion modeling reported here builds on earlier studies of MW activated C/H/Ar plasmas used for MCD growth containing 4.4%CH_4/88.6%H_2/7%Ar,[26] and of inert gas-rich plasmas such as are used for UNCD film growth.[27] Previous theoretical studies of Ar-rich C/H/Ar plasmas have generally involved use of 0 or 1D kinetic models,[28,29] with particular focus on UNCD conditions and mechanisms for forming the soot particles observed at the periphery of such Ar-rich plasmas.[28] The present studies do not consider possible effects of nanoparticles on the plasma parameters and kinetics, but succeed in reproducing the measured radical column densities and profiles well, and thereby offer new and systematic understanding of the effects of progressive replacement of H_2 by Ar (or other rare gas) on the chemistry and characteristics of MW activated C/H/Ar plasmas.

II. EXPERIMENTAL

The procedures for CRDS and OES measurements have both been described previously.[20,23] 2.45 GHz radiation exiting a rectangular waveguide is converted into the TM_{01} mode and coupled into a purpose-designed and built cylindrical MW-PECVD reactor, comprising two parts separated by a centrally mounted quartz window. The lower chamber is vacuum-sealed and contains the plasma. The premixed CH_4/H_2/Ar process gas mixture is fed through two diametrically opposed inlets located beneath the quartz window and is exhausted through the baseplate. The MW radiation partially ionizes and dissociates the gas mixture. "Active" species are produced, some of which react on the Mo substrate (diameter, $d=3$ cm) to form a polycrystalline diamond film. For future reference,"base" discharge conditions for the present studies were: total pressure, $p=150$ Torr, input power, $P=1.0$ kW and a total flow rate $F_{total}=525$ standard cm^3 per minute (sccm). We define the proportion of each reagent in the gas mixture at the inlet of the reactor as a mole fraction X_0 of F_{total}. Base conditions for the present studies are: $X_0(CH_4)=0.5\%$ [i.e., $F(CH_4)=2.7$ sccm in $F_{total}=525$ sccm], $X_0(H_2)=14.7\%$ [$F(H_2)=77$ sccm], with the balance $X_0(Ar)=84.8\%$ [$F(Ar)=445$ sccm]. When investigating the effects of varying $X_0(H_2)$ and/or $X_0(CH_4)$, any variation away from this base condition was compensated by a corresponding adjustment in $X_0(Ar)$ so as to maintain F_{total} at 525 sccm. As discussed in detail later, it was necessary to reduce P (as low as 0.5 kW) when operating with the low H_2 fractions appropriate for UNCD growth (e.g., 0.5%CH_4/1%H_2/balance Ar).

The MW-PECVD reactor is coupled to tubular stainless steel side-arms by flexible knife-edge bellows assemblies. These side-arms, which are terminated with kinematic mounts that hold high-reflectivity CRDS mirrors, are mounted rigidly on a platform that supports the laser beam steering optics, and the complete optical assembly (including the CRDS mirrors and the detector) can be translated vertically relative to the fixed MW reactor — thereby enabling spatially resolved, line-of-sight column density measurements with sub-mm precision, as a function of z, the vertical distance above the top surface of the Mo substrate. The required excitation wavelengths are provided by a Nd:YAG pumped dye laser (Continuum Surelite III plus Spectra-Physics PDL-3, bandwidth ~0.1 cm^{-1}) operating at a repetition rate of 10 Hz and wavelengths of ~515, ~431, and ~656.2 nm for detection of, respectively, $C_2(a,\ v=0)$ and CH ($X,\ v=0$) radicals, and H($n=2$) atoms. Transmitted light intensities are monitored beyond the exit mirror with a photomultiplier tube. Data collection and analysis used custom-written LABVIEW programs, communicating with a digital oscilloscope (LeCroy Waverunner 64Xi, 4 channel, 600 MHz, 10 Gs/s) via an Ethernet connection.

Optical emission from a localized volume somewhat below the center of the luminous plasma ball was viewed along an axis orthogonal to the laser probe axis, through a ~9 mm diameter aperture located behind a glass view port that was vacuum sealed to a flange mounted on the reactor wall. Emission passing through this aperture was focused onto one end of a quartz multicore optical fiber. Light exiting the fiber was dispersed through a monochromator equipped with a cooled (to 10 °C) charge coupled device (CCD) strip detector (Oriel Instaspec IV, 600 lines mm^{-1} ruled grating) that provides a spectral resolution better than 1 nm over a 300 nm portion of the total emission spectrum. Typical CCD exposure times for measurements of the plasma emission (and the background, recorded with the plasma emission blocked) were 20 ms, and the data averaged 1000 times.

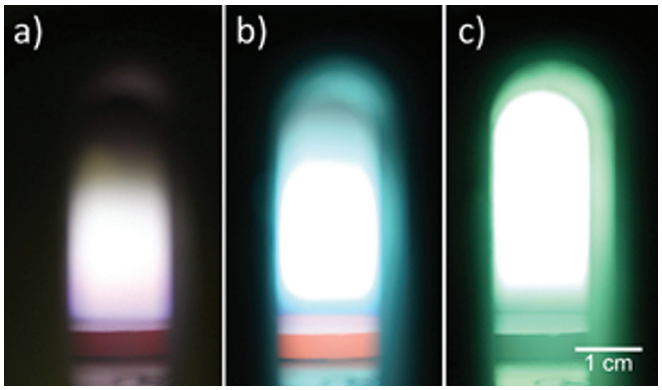

FIG. 1. (Color online) Images of the plasma ball seen through the front view port of the reactor when operating with the following process conditions: $p = 150$ Torr, $P = 1.0$ kW, $X_0(CH_4) = 0.5\%$, $X_0(H_2) = 92\%$ (a), 36.9% (b), and 9.2% (c), balance Ar.

III. RESULTS

As Fig. 1(a) shows, the plasma under representative MCD growth conditions (i.e., 0.5%CH_4/92%H_2/7.5%Ar, $p = 150$ Torr, $P = 1.0$ kW) has a mauve/purple color and is localized in a relatively small volume above the substrate. Progressive substitution of H_2 by Ar causes (i) an obvious increase in the size of the luminous volume and (ii) changes in the color of the emission, which turns paler and greener [$X_0(H_2) = 36.9\%$, Fig. 1(b)] and then intensely white/green [$X_0(H_2) = 9.2\%$, Fig. 1(c)]. The substrate temperature (T_{sub}) also evolves, first increasing, then declining, as $X_0(H_2)$ is decreased. This is shown in Fig. 2, along with estimates of the power loss to the wall and to the base of the reactor, as functions of $X_0(H_2)$, as determined by measuring the temperature rise in the cooling water. The aim of the present study is to account for all of these changes, by a combination of experimental measurements and modeling. In the remainder of Sec. III we describe determinations of the gas temperature in the plasma region, absolute (and relative) density measurements of selected radical species as a function of process condition [e.g., varying $X_0(H_2)$, $X_0(CH_4)$, P, and p], and compare the spatial distributions of these selected species measured at high and low H_2 mole fractions [$X_0(H_2) = 88.6\%$ and 14.7%, respectively]. The measured gas phase densities and temperatures match well with the predictions of 2D modeling studies of C/H/Ar plasmas — Sec. IV —wherein we also compare the measured and calculated power dissipation pathways, and their sensitivity to $X_0(H_2)$. The good agreement between experiment and theory not only serves to validate the modeling, but also lends credence to the broader insights provided by the latter regarding the essential physics underpinning these thermally dominated, high pressure C/H/Ar plasmas and the ways in which changes in plasma conditions will influence subsequent diamond growth.

A. CRDS spectra and gas temperature determinations in the plasma region

As shown previously,[23] CRDS spectra of the $C_2(d^3\Pi_g \leftarrow a^3\Pi_u)$ (0,0) band can provide a convenient probe of T_{gas} in the hot plasma region. Figure 3 shows a portion of this spectrum measured along a column through the plasma at one particular height above the substrate surface ($z = 9.5$ mm), recorded for a range of plasma conditions. The three lines at lower wavenumber correspond to R branch transitions involving low J rotational levels, whereas the features at higher wavenumber (the 19246.9 cm^{-1} feature is a blend of two strong lines) are associated with transitions between high J levels in the P branch. The ratio of the low and high J line intensities thus gives an immediate visual impression of the $C_2(a)$ rotational temperature, T_{rot}, which can be quantified by fitting the spectral line positions and intensities using PGOPHER[30] and appropriate spectroscopic constants for the a and d states of C_2.[31] The spectra shown in Fig. 3 were measured for (a) typical MCD growth conditions (i.e., 4.4%CH_4/88.6%H_2/7%Ar, $p = 150$ Torr, $P = 1.5$ kW), (b) the present base conditions, and (c) representative UNCD growth conditions (0.5%CH_4/1%H_2/98.5%Ar, $p = 150$ Torr, $P = 0.5$ kW). The most striking feature of these spectra is their similarity; the best fit rotational temperature in each case is $T_{rot} \sim 3000$ K. The top and bottom traces in Fig. 3 are PGOPHER simulations, assuming $T_{rot} = 3000$ and 2000 K,

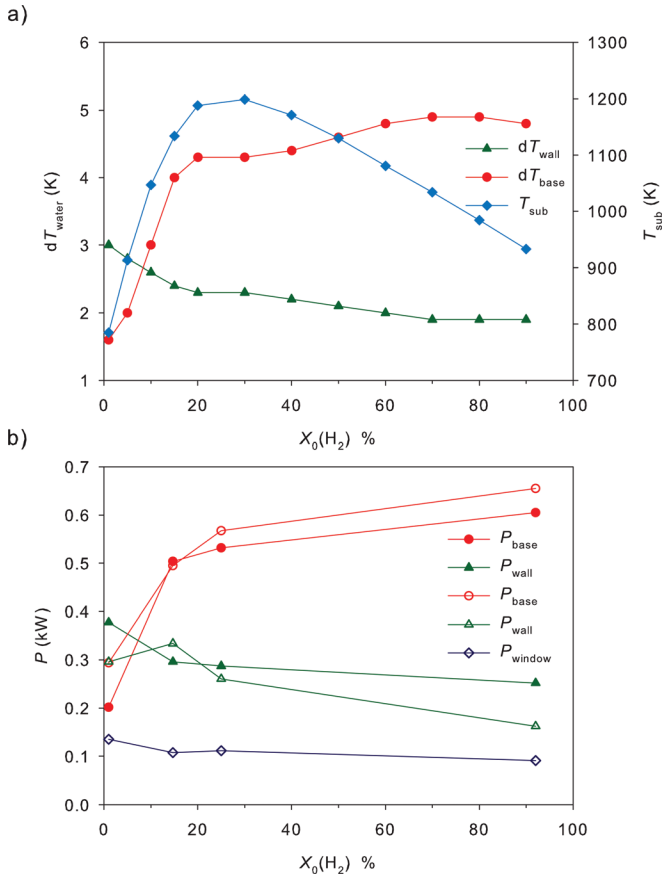

FIG. 2. (Color online) (a) Measured temperature rises in the cooling water flowing (at a rate of 1 l min^{-1}) through the sidewalls (dT_{wall}) and the base (dT_{base}) of the MW PECVD reactor operating at $P = 1.0$ kW, $p = 150$ Torr, with $X_0(CH_4) = 0.5\%$ at different $X_0(H_2)$. (b) Comparison of the measured (filled symbols) and calculated (open symbols) contributions to the overall power ($P = 1.0$ kW) dissipation, as a function of $X_0(H_2)$. The experimental data shown in this plot have been scaled by a factor $a = 2$, while the calculated data for $X_0(H_2) = 1\%$ and 88.6% have been scaled by factors of 2 and 0.67, respectively, in recognition of the different P values at which the modeling was performed.

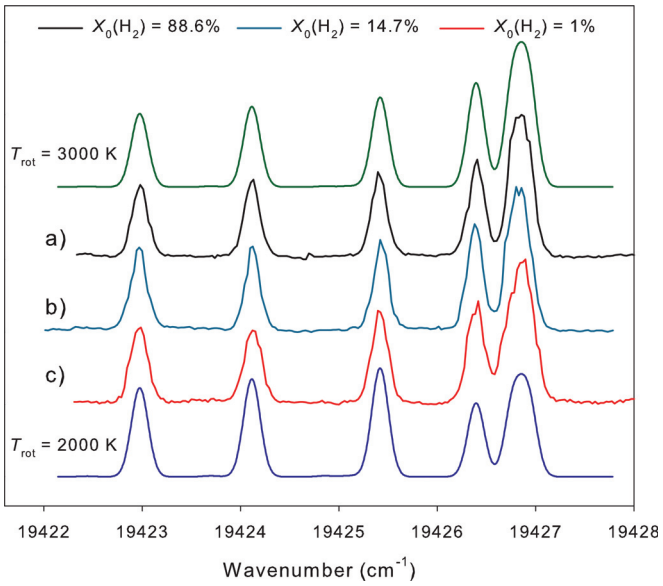

FIG. 3. (Color online) CRDS spectra of part of the $C_2(d^3\Pi_g \leftarrow a^3\Pi_u)$ (0,0) band measured for (a) typical MCD growth conditions (4.4%CH_4/88.6%H_2/7%Ar, $p = 150$ Torr, $P = 1.5$ kW), (b) the present base conditions (0.5%CH_4/14.7%H_2/84.8%Ar, $p = 150$ Torr, $P = 1$ kW), and (c) representative UNCD growth conditions (0.5%CH_4/1%H_2/98.5%Ar, $p = 150$ Torr, $P = 0.5$ kW). Straddling these three traces are PGOPHER simulations of the relevant part of the overall band contour assuming $T_{rot} = 3000$ K (above) and 2000 K (below).

which serve to demonstrate the reliability of these temperature estimates. The efficiency of rotational-translational energy transfer processes at $p = 150$ Torr ensures local thermodynamic equilibrium and validates the assumption that T_{rot} is a good measure of the local T_{gas}. As shown previously,[26] the local gas temperature varies greatly along the probed column; it is close to room temperature near the water cooled reactor walls and maximizes in the center of the plasma ball. Again, as in the earlier studies of 4.4%CH_4/88.6%H_2/7%Ar plasmas (with $p = 150$ Torr and $P = 1.5$ kW), the high T_{rot} values derived from analysis of the $C_2(d \leftarrow a)$ absorption spectra imply that these radical species are concentrated in the hot plasma ball. The spectra shown in Fig. 3 also illustrate that T_{gas} in the hot region is rather insensitive to changes in H_2/Ar ratio and thus, as we show below, to the plasma volume, the mean power density and the electron temperature, T_e.

Several groups have previously reported T_{rot} values against which the present data can be compared. Much lower T_{rot} values (1150–1300 K) were reported from an early broadband absorption study of $C_2(a)$ radicals in 1%CH_4/2%H_2/97%Ar plasmas ($50 \leq p \leq 100$ Torr, $0.50 \leq P \leq 1.5$ kW),[32] but our re-analysis of the published spectra using PGOPHER suggests that the T_{rot} values for these spectra are in fact ~3000 K. Rabeau *et al.*[33] reported CRD spectra for $C_2(a)$ radicals in plasmas containing 1%CH_4, H_2 fractions ranging from 0%–14%, with the balance Ar, operating at $p = 90$ Torr and $P = 2.1$ kW. As in the present work, T_{rot} values ~3000 K were returned for all conditions. Lombardi *et al.*[34] used band contour analysis methods to estimate T_{rot} values from both broadband absorption and emission spectra of C_2 and (after deliberate addition of trace quantities of N_2) CN radicals in 1%CH_4/(2–7%)H_2/balance Ar plasmas operating at a range of MW powers, $P \leq 0.8$ kW, and pressures, $p \leq 150$ Torr. The values so determined spanned the range 3000 up to ~4200 K, depending on spectral carrier but, again, showed no clear systematic variation with changes in H_2/Ar fraction or P.

B. Column density measurements as functions of process conditions

Column densities of $C_2(a, v = 0)$ and $CH(X, v = 0)$ radicals, and $H(n = 2)$ atoms – henceforth represented as $\{C_2(a, v = 0)\}$, $\{CH(X, v = 0)\}$, and $\{H(n = 2)\}$, respectively – were obtained from CRDS measurements of portions of the $C_2(d–a)$, $CH(A–X)$, and $H(n = 3–n = 2)$ absorption spectra as described previously.[23] Figure 4 shows column densities for the two radical species (left hand axis) and $H(n = 2)$ atoms (right hand axis), measured at $z = 9.5$ mm, starting from the present base conditions and, in each case, varying one parameter.

Figure 4(a) shows the changes in column density that occur as a result of varying $X_0(H_2)$ with a compensatory change of $X_0(Ar)$ to conserve F_{total}. Our previous study[23] showed the column densities of all three target species increasing as $X_0(H_2)$ was decreased from 95.6 to 42.5% [i.e., $X_0(Ar)$ increased from 0% and 53.1%], with that for $C_2(a)$ showing the steepest growth: the $\{C_2(a, v = 0)\}/\{CH(X, v = 0)\}$ ratio increased > threefold across this range of $X_0(H_2)$. As Fig. 4(a) shows, such trends continue as $X_0(H_2)$ is decreased further. At the present base conditions ($X_0(H_2) = 14.7\%$), $\{C_2(a, v = 0)\}$, and $\{CH(X, v = 0)\}$ are comparable (at $z = 9.5$ mm). Upon decreasing $X_0(H_2)$ further, $\{CH(X, v = 0)\}$ plateaus and then falls whereas $\{C_2(a, v = 0)\}$ increases steeply. $\{H(n = 2)\}$ also increases ~fourfold as $X_0(H_2)$ decreases from ~50% to ~10%. Once $X_0(H_2) < 10\%$ the plasma ball has become so large that it is no longer safe to operate the reactor at the base power of 1.0 kW. Nonetheless, it is possible to investigate plasmas with yet lower H_2 content by operating at reduced P. Figure 4(a) includes four $\{C_2(a, v = 0)\}$ data points measured at $z = 9.5$ mm with $X_0(H_2) = 1$, 5, 10, 15% and $P = 0.5$ kW. These show a continued rise in $\{C_2(a, v = 0)\}$ with decreasing $X_0(H_2)$, in apparent contradiction of the earlier findings of Rabeau *et al.*[33] who observed $\{C_2(a, v = 0)\}$ peaking at $X_0(Ar)$ ~95%. We note, however, that the sooty nature of plasmas operating with very low $X_0(H_2)$ presents a challenge to detailed column density measurements, and that the trends observed are likely to be sensitive to the reactor configuration, changes in plasma volume (and/or location with respect to the substrate surface) with $X_0(H_2)$, and the choice of z.

Figure 4(b) shows the effect of varying $X_0(CH_4)$ from zero [i.e., a hydrocarbon-free $X_0(H_2) = 14.7\%$ in Ar plasma] to 2% [with, again, a compensatory adjustment of $F(Ar)$ to ensure constant F_{total}]. The observed trends in $\{C_2(a, v = 0)\}$, $\{CH(X, v = 0)\}$, and $\{H(n = 2)\}$ with increasing $X_0(CH_4)$ resemble those observed for the standard MCD plasma, but differ in detail. As before,[23] $\{C_2(a)\}$ scales approximately linearly with $X_0(CH_4)$, whereas $\{CH(X)\}$ increases less steeply. Both radical column densities are about an order of magnitude greater than in the case of the standard MCD plasma,

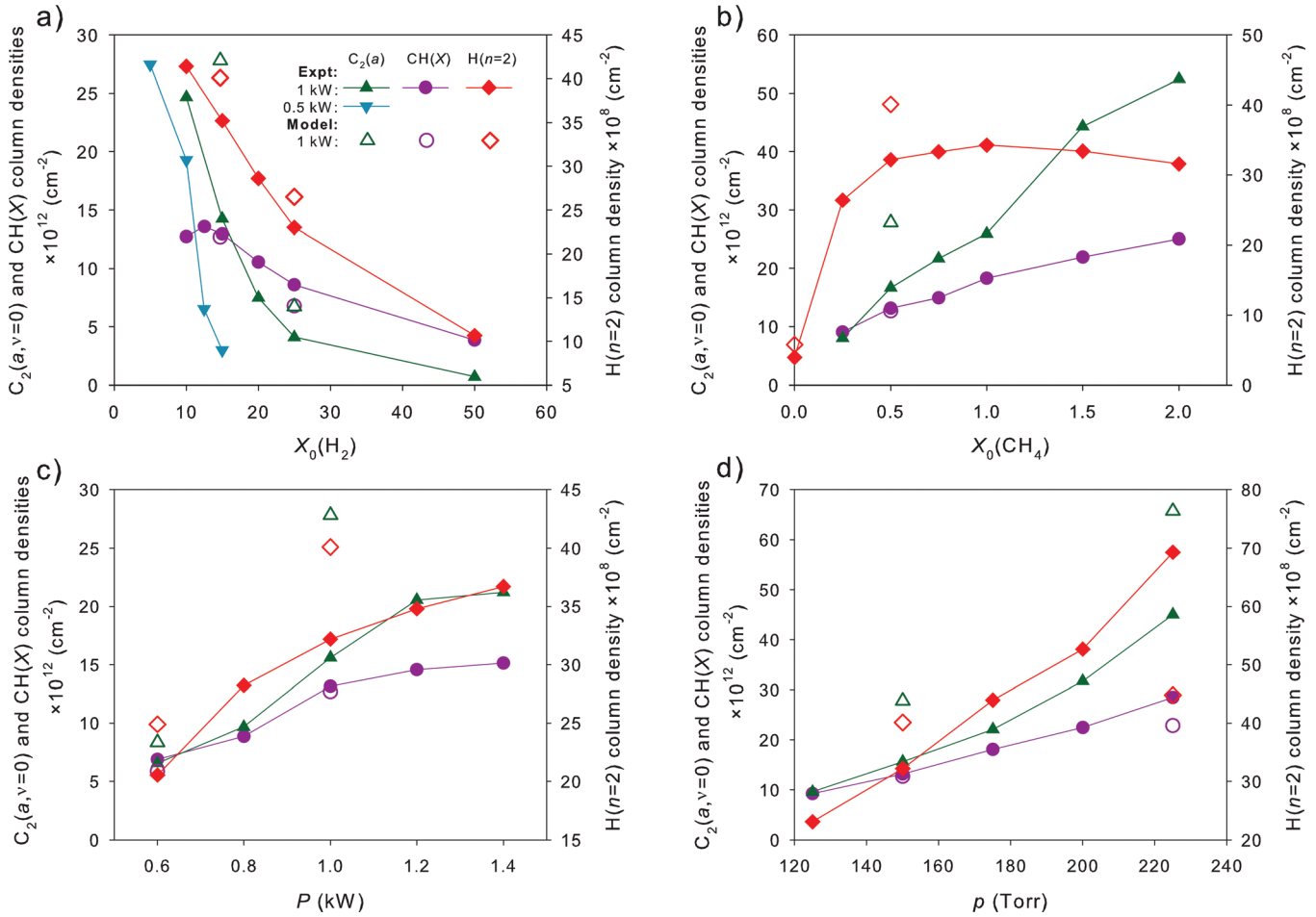

FIG. 4. (Color online) Filled symbols: Column densities of $C_2(a, v=0)$ and $CH(X, v=0)$ radicals (left hand scale), and of $H(n=2)$ atoms (right hand scale) measured at $z=9.5$ mm, plotted as functions of (a) $X_0(H_2)$, (b) $X_0(CH_4)$, (c) applied MW power, P and (d) total pressure, p. When recording the data in (a) and (b) $X_0(Ar)$ was adjusted in a compensatory manner to ensure $F_{total}=525$ sccm. The open symbols in each plot show values for the corresponding quantities returned by the 2D model calculations for $P=1$ kW.

however. $\{H(n=2)\}$ shows an ~eightfold increase upon introducing even trace amounts (0.25%) of CH_4. As previously, this reflects the changing identity of the dominant ion (H_3^+ and ArH^+ in the case of the H_2/Ar plasma, $C_yH_x^+$ in the case of C/H/Ar plasmas [e.g., $C_2H_x^+$ $(x=2, 3)$ for the base and H_2-rich gas mixtures, C_3H^+ and $C_2H_x^+$ $(x=1-3)$ for UNCD plasmas] and the concomitant increases in T_e that occur upon adding even trace amounts of CH_4. The increase in the average value of T_e returned by the 2D model (1.28 eV for 0% CH_4, 1.74 eV for 0.5% CH_4) is significant; it has substantial impact on the ionization/recombination balance of the charged plasma species, as discussed in Sec. IV.

Figures 4(c) and 4(d) show that, under the present base conditions, $\{C_2(a, v=0)\}$, $\{CH(X, v=0)\}$ and $\{H(n=2)\}$ all increase with increasing P (from 0.6 to 1.4 kW) and p (from 125 to 225 Torr). In both cases, the relative increase in $\{C_2(a, v=0)\}$ is greater than that in $\{CH(X, v=0)\}$ or $\{H(n=2)\}$.

Also shown in Fig. 4 (open symbols) are the values returned by the 2D modeling, after summing the calculated number densities to obtain the corresponding column densities. The calculated trends are discussed in Sec. IV but, simply by inspecting Fig. 4, it is clear that the modeling succeeds in capturing the absolute column densities, and their variation with process conditions [in all but the case of the pressure dependence of $\{H(n=2)\}$].

Figure 5 shows the z dependence of $\{C_2(a, v=0)\}$, $\{CH(X, v=0)\}$ and $\{H(n=2)\}$ measured for the present base conditions. These show notable differences from the corresponding distributions measured for representative MCD growth conditions (4.4%CH_4/88.6%H_2/7%Ar, $F_{total}=565$ sccm, $p=150$ Torr, $P=1.5$ kW),[23] which are reproduced in Fig. 5 also. First, we note that the peak column densities of all three target species are substantially higher in the Ar-rich plasma, despite the fact that the MCD data used in this comparison involved a higher $X_0(CH_4)$ (4.4% cf. 0.5%) and higher MW power (1.5 kW cf. 1.0 kW). Second, all three distributions peak at larger z in the Ar-rich plasma than in the representative MCD plasma, consistent with the visible expansion of the luminous plasma ball upon decreasing $X_0(H_2)$ in Fig. 1. Because of this plasma expansion, it is clear that the $\{C_2(a, v=0)\}$ and $\{CH(X, v=0\}$ measurements reported in Fig. 4 have sampled z values below the plasma center. Finally we note that, as in the case of the MCD plasma, the $\{H(n=2)\}$ distribution in the present base conditions peaks at smaller z than the two radical density distributions, as expected given that the $H(n=2)$ density depends on a convolution of the local densities of $H(n=1)$

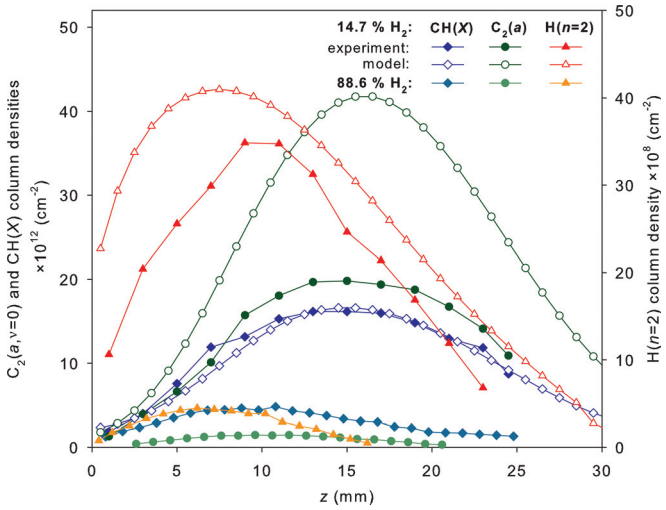

FIG. 5. (Color online) Measured and calculated (filled and open symbols, respectively) column densities of $C_2(a,\ v=0)$, $CH(X,\ v=0)$ and $H(n=2)$ plotted as a function of z for the present base conditions (0.5%CH_4/14.7%H_2/84.8%Ar, $p=150$ Torr, $P=1$ kW). Also shown, for comparison, are the $C_2(a,\ v=0)$, $CH(X,\ v=0)$ and $H(n=2)$ column densities measured for typical MCD growth conditions (4.4%CH_4/88.6%H_2/7%Ar, $p=150$ Torr, $P=1.5$ kW, from Ref. 23).

atoms and of suitably energetic electrons (and electronically excited species, e.g., Ar*).[23]

C. Optical emission measurements

Optical emission spectra from the present base plasma were qualitatively similar to those reported previously for the case of Ar-rich C/H/Ar plasmas,[27] exhibiting features attributable to $CH(A)$, $C_2(d)$, and $C_3(A)$ state radicals (at 431.4, 516.5, and ~405 nm, respectively) and to $H(n=3$ and 4) atoms (H_α and H_β, at 656.3 and 486.1 nm). The process condition dependence of each of these emissions was investigated.

The optical emission studies of the effects of decreasing $X_0(H_2)$ from ~50% to 5% [Fig. 6(a)] show similar trends to those observed by CRDS [Fig. 4(a)]. The $CH(A–X)$ emission intensity maximizes at $X_0(H_2)$ ~10% and then declines if $X_0(H_2)$ is decreased further. The emissions from $C_2(d)$ and $C_3(A)$ radicals, in contrast, continue to increase to the lowest $X_0(H_2)$ investigated, with the latter showing the steeper rate of increase. The H_α and H_β emission intensities show qualitatively similar $X_0(H_2)$ dependencies to the $CH(A–X)$ emission, peaking at $X_0(H_2)$ ~10%. The $I(H_\beta)/I(H_\alpha)$ ratio changes little across this range but, again, several plasma parameters are varying simultaneously and it does not follow that T_e is

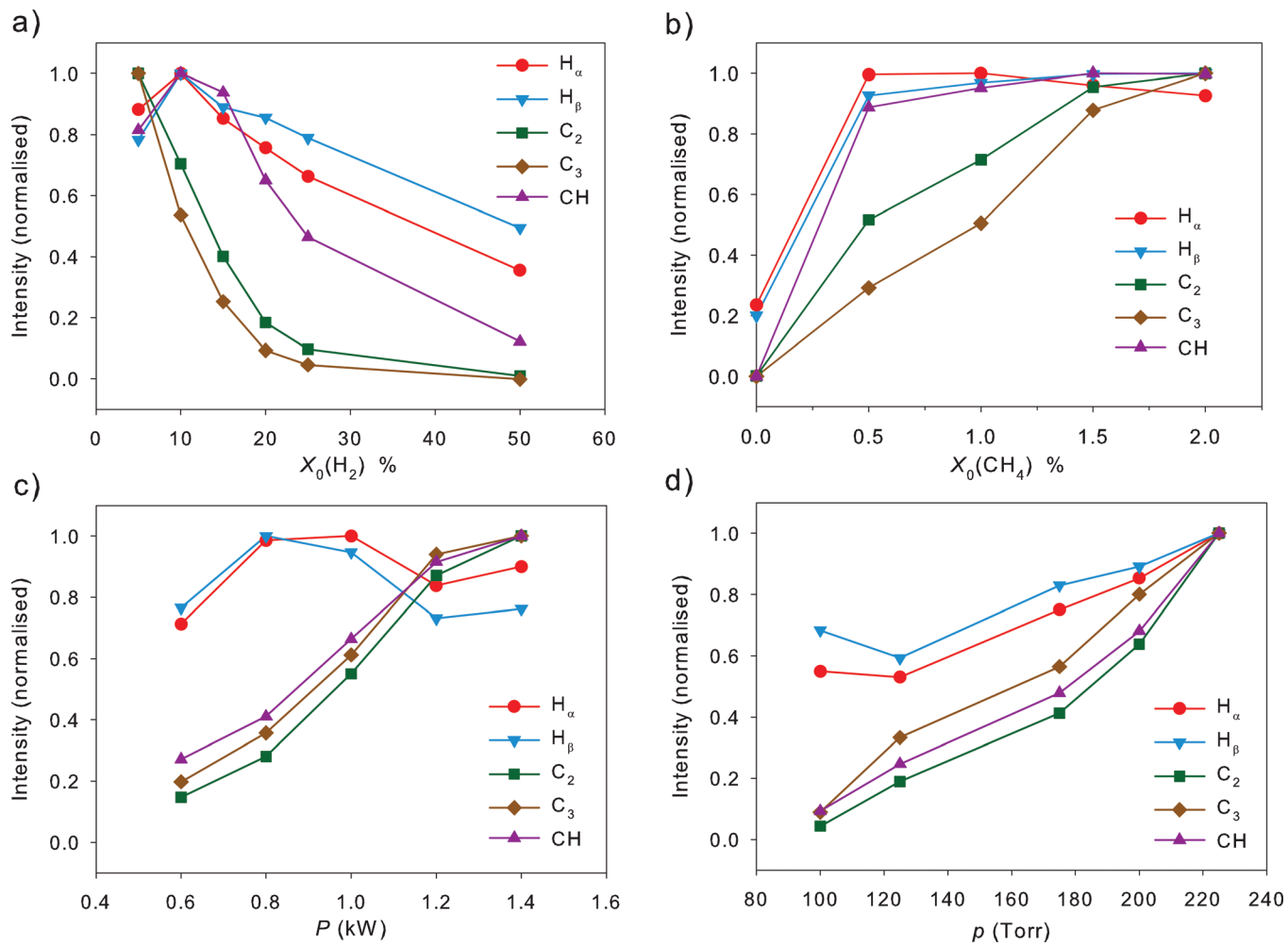

FIG. 6. (Color online) Normalized relative H_α, $CH(A–X)$, $C_2(d–a)$ and $C_3(A–X)$ emission intensities plotted as functions of (a) $X_0(H_2)$, (b) $X_0(CH_4)$, (c) P, and (d) p. The uncertainties in the normalized emission intensities from one spectrum to another are smaller than the displayed data points.

insensitive to the H_2 content. Once again, the 2D model returns similar $\{H(n=3)\}/\{H(n=2)\}$ ratios: $5.5\times10^6[cm^{-2}]/2.25\times10^9[cm^{-2}]$, $1.4\times10^7[cm^{-2}]/4\times10^9[cm^{-2}]$, and $1.3\times10^7[cm^{-2}]/2.7\times10^9[cm^{-2}]$ at $X_0(H_2)=1\%$, 14.7%, and 25%, despite the different T_e values prevailing in the three environments: 2.45, 1.74, and 1.67 eV, respectively. The model also reproduces the observed "explosion" of C_3 emission intensity upon reducing $X_0(H_2)$. This intensity is estimated by convoluting the local densities of C_3 radicals and electrons, i.e., $\sum_r[C_3](r)\cdot n_e(r)\cdot dr$, yielding relative values 296: 6.6: 1 for $X_0(H_2)=1\%$, 14.7%, and 25%. Changes in $[C_3]$ are largely responsible for this explosion; the calculated electron column densities, 3.5×10^{12}, 1.5×10^{12}, and 1.1×10^{12} cm^{-2} at the respective $X_0(H_2)$ values, only differ by factors of 3.2: 1.4: 1.

The normalized H_α emission measured at $z\sim10$ mm shows a step increase upon introducing CH_4, but thereafter declines gently as $X_0(CH_4)$ is increased further (up to 2%), as shown in Fig. 6(b). Such behavior mimics that observed in the present CRDS measurements [Fig. 4(b)], and in the earlier studies of H_2-rich C/H/Ar plasmas.[23] T_e increases markedly when CH_4 is added to a preexisting H_2/Ar plasma (Sec. III B) and this increase alters the balance of ionization and recombination reactions in the plasma. A significant change in T_e would traditionally be expected to reveal itself by a change in the relative intensities of the H_α and H_β emissions [i.e., the $I(H_\beta)/I(H_\alpha)$ ratio]. Yet, as Fig. 6(b) shows, this ratio changes little on CH_4 addition. This apparent contradiction is explained by the current 2D modeling, which demonstrates that invariance of the $I(H_\beta)/I(H_\alpha)$ ratio (at any given z) does not necessarily imply near constancy of T_e if, as here, several plasma parameters (e.g., T_e, n_e, the excited argon and H atom concentrations, their respective spatial distributions, the plasma volume, etc.) are varied simultaneously. For example, the 2D model returns broadly similar $H(n=3)$ to $H(n=2)$ column density ratios at $z=9.5$ mm – $\{H(n=3)\}/\{H(n=2)\}=1.7\times10^6[cm^{-2}]/5.8\times10^8[cm^{-2}]$ and $1.4\times10^7[cm^{-2}]/4\times10^9[cm^{-2}]$ – for $X_0(CH_4)=0$ and 0.5%, respectively, despite T_e increasing from 1.28 eV (0%CH_4) to 1.74 eV (0.5%CH_4). Note that the model succeeds in capturing not just the invariance of the $\{H(n=3)\}/\{H(n=2)\}$ ratio, but also the observed ~fivefold jump in $I(H_\alpha)$ upon adding 0.5% CH_4 [cf. the predicted ~eightfold increase in $\{H(n=3)\}$].

Figure 6(c) shows that the H_α, $CH(A)$, $C_2(d)$, and $C_3(A)$ emission intensities all increase with increasing input power for the present base gas composition — as expected given that increasing P leads to increased densities of $H(n=1)$ atoms (the reactions of which drive carbon radical formation) and of electrons (collisions with which drive the electronic excitations responsible for the observed emissions). Figure 6(d) shows the variation in normalized species emissions as a function of total pressure over the range $100\le p\le225$ Torr. The $CH(A)$, $C_2(d)$, and $C_3(A)$ emission intensities all increase with p, reflecting the thermally driven origin of the $CH(X)$, $C_2(a)$, and $C_3(X)$ radicals from which they derive. The H_α and H_β emission intensities also increase, but only by factors of ~2. Again, the 2D modeling reproduces the measured P and p variations for the excited $CH(A)$, $C_2(d)$, and $C_3(A)$ radicals, but fails to reproduce the p dependence of the H_α emission. For example, convoluting the calculated C_3 column densities with the corresponding electron densities yields values of 2×10^{25} cm^{-5} (for the present base conditions, $p=150$ Torr, $P=1$ kW), 5.2×10^{24} cm^{-5} for $p=150$ Torr, $P=0.6$ kW and 4.2×10^{25} cm^{-5} for $p=225$ Torr, $P=1$ kW. The calculated $H(n=3)$ column densities for these same three conditions are, respectively, 1.4×10^7 cm^{-2}, 8.8×10^6 cm^{-2}, and 8.7×10^6 cm^{-2}.

IV. MODELING THE VARIATION IN PLASMA PARAMETERS AND SPECIES DISTRIBUTIONS IN H_2-RICH AND Ar-RICH C/H/Ar PLASMAS

A. The 2D model

Details of the 2D(r, z) model used to describe essential processes occurring in the present MW PECVD reactor have been reported previously.[26] Briefly, the model assumes cylindrical symmetry, with coordinates r (the radial distance from the central axis of the chamber) and z [the axial (vertical) height above the substrate surface], a reactor radius, $R_r=6$ cm and height, $h=6$ cm. The local electron energy distribution function is calculated for different gas mixtures and different plasma conditions, with the volume V in which the MW power is absorbed incorporated as a parameter — thereby allowing estimation of the reduced electric field and the electron temperature (T_e) in the plasma region for any given value of input power P. As noted previously,[26] the reduced electric field and the average T_e both tend to be rather uniform throughout the plasma core region. For example, Hassouni *et al.*[35] showed T_e declining by ~10% with increasing distance from the substrate in the case of H_2-rich plasmas. For consistency, we persist with the earlier assumption[26] that T_e is uniform throughout the H_2-rich plasmas but, in the case of Ar-dominated [i.e., $X_0(H_2)<X_0(Ar)$] plasmas, the present modeling assumes a 20% decline in T_e — parameterized as a ± 10% variation from the average T_e at the plasma center. Reabsorption of H and Ar resonance line emissions was treated approximately using an escape factor (θ) approach wherein, in the case of an optically thick plasma, relevant radiative decay rates A were replaced by $A\times\theta$. For the present base calculations $\theta\sim0.1$ was assumed both for the $H(n=2,3)\rightarrow H(n=1)+h\nu$ and $Ar^{**}\rightarrow Ar+h\nu$ resonance lines. 2D model calculations show that radiative loss has a relatively small affect on the overall plasma power balance, accounting for < 7% of the total input power for mixtures with $X_0(H_2)\ge14.7\%$. This fraction can reach ~20%–30% in the case of UNCD (e.g., 0.5%CH_4/1%H_2/98.5%Ar) plasmas however, as a result of the greatly increased emission from C_yH_x species (e.g., C_3, C_2).

As in our previous work,[26] this study of MW activated C/H/Ar gas mixtures employs a base chemical mechanism involving 38 species and >240 reactions. The set of nonstationary conservation equations for mass, momentum, energy, and species concentrations are solved numerically by a finite difference method in (r, z) coordinates. The 2D model takes into account the changes in plasma parameters and conditions as a result of variations in reactor parameters like

p, P, $X_0(CH_4)$, $X_0(H_2)$, and $X_0(Ar)$, the thermal conductivity of the gas mixture, etc.

B. Effects of progressive replacement of H_2 by Ar on C/H/Ar plasma parameters and species distributions

Figure 7 shows 2D (r, z) false color plots of the calculated spatial distributions of T_{gas} and the H atom mole fraction, $X(H)$, for two different gas mixtures: (a) 0.5%CH_4/14.7%H_2/Ar (i.e., the present base mixture) and (b) 0.5%CH_4/1%H_2/Ar, both at $p=150$ Torr, and activated by MW powers of, respectively, 0.6 and 0.5 kW. Note that the MW power considered in Fig. 7(a), $P=0.6$ kW, is only 60% of the value used in the present experimental studies, but comparing plasmas excited with similar MW powers enables a clearer visualization of the differences – most notably the obvious expansion of the plasma, and the extremely high degree of H_2 dissociation at typical UNCD conditions [i.e., $X_0(H_2)=1\%$, Fig. 7(b)]. Comparing these two figures, we see that a 14.7-fold increase in the input $X_0(H_2)$ causes only a modest (~twofold) increase in the H atom mole fraction — from $X(H)$ ~2% [Fig. 7(b), under conditions where $X_0(H_2)$ is only 1%] to ~4.5% when $X_0(H_2)=14.7\%$ [Fig. 7(a)]. Note that the total $X(H)$ achievable under UNCD conditions would involve comparable contributions from H_2 and CH_4, i.e., 2% [from $X_0(H_2)=1\%$] plus either 1.5% [from $X_0(CH_4)=0.5\%$ in the case of the hypothetical conversion $CH_4 \rightarrow 0.5C_2H_2+3H$] or plus 2% in the case that $X_0(CH_4)=0.5\%$ is fully dissociated to $C_x/x+4H$ ($x=1-3$).

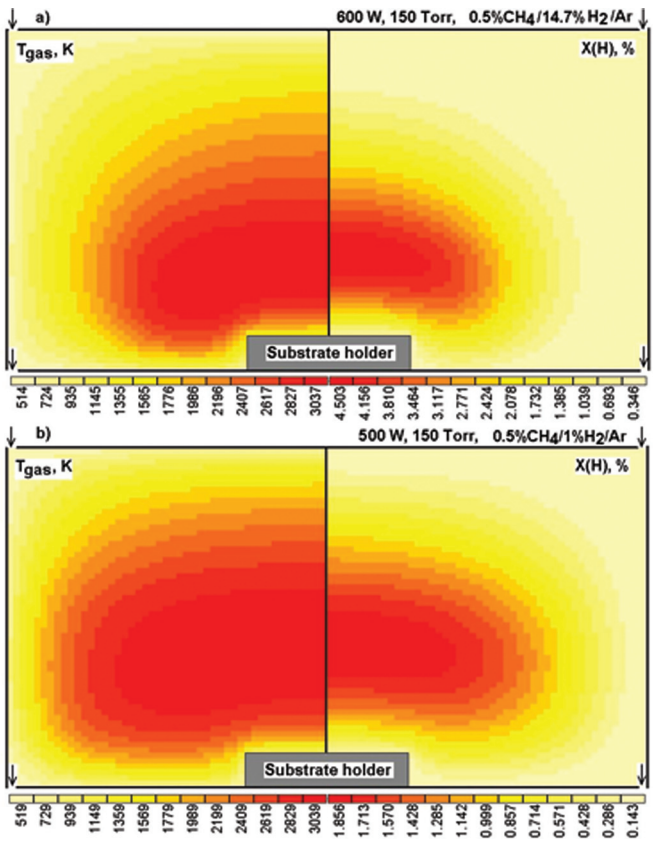

FIG. 7. (Color online) 2D(r,z) model distributions of T_{gas} (in K, left) and H atom mole fraction $X(H)$ (%, right) for (a) the base gas mixture (0.5%CH_4/14.7%H_2/84.8%Ar, $p=150$ Torr and $P=0.6$ kW) and (b) a representative gas mixture for UNCD growth (0.5%CH_4/1%H_2/98.5%Ar, $p=150$ Torr, $P=0.5$ kW). The vertical (z) and radial (R_r) dimension of the simulated reactor is 6 cm.

One of the major aims of the present study was to trace the changes in plasma parameters and diamond deposition conditions that accompany the progressive replacement of H_2 by Ar, across a wide range of process gas mixtures (from 0.5%CH_4 in H_2 through to 0.5%CH_4/1%H_2/balance Ar). Figure 8 serves to summarize some of the key changes. One key difference is the plasma volume, which is much smaller for H_2-rich conditions (V ~35 cm^3 in 4.4%CH_4/88.6%H_2/7%Ar, even at an input power $P=1.5$ kW) than under UNCD [$X_0(H_2)=1\%$] conditions – for which we estimate V ~210 cm^3, at just $P=0.5$ kW. The central zone of the plasma is correspondingly further from the substrate in the latter case ($z_C \sim 20$ mm, cf. ~10 mm in the case of the H_2-rich plasma). This difference is reflected in the relative increase in the power dissipated via the reactor walls (rather than the base) under Ar-rich conditions (recall Fig. 2). Notwithstanding the much higher average power densities, Q, and higher reduced electric fields prevailing in the H_2-rich plasma, the 2D model returns a notably lower electron temperature (T_e ~1.31 eV) in this environment[26] than in the case of the Ar-rich UNCD gas mixture (T_e ~2.45 eV).

These differences can be understood by tracing the complex balance of ionization versus recombination reactions for the charged species, and recognizing that most of the input power under H_2-rich conditions is expended in rotational and vibrational excitation of H_2, and subsequent rotation→translation and vibration→translation relaxation. Such processes account for >90% of the total absorbed MW power density when $X_0(H_2)>85\%$,[26] and typically result in average power densities in the range $10 \le Q \le 50$ W cm^{-3}. Under UNCD conditions, the energy absorbed by the electrons is expended on rovibrational excitation of H_2 and C_yH_x species, and in elastic collisions with Ar, H, and H_2,[27] but the density of

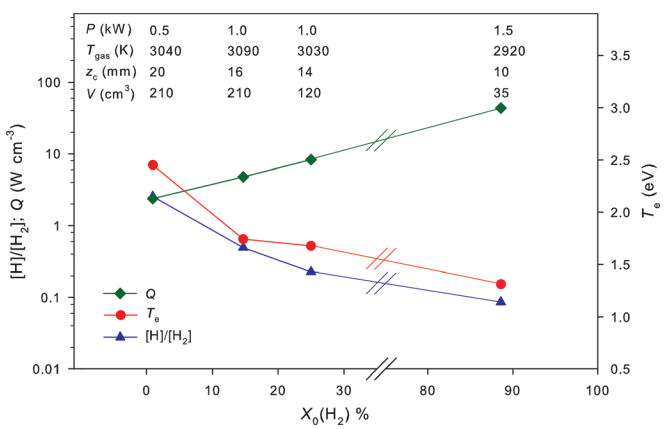

FIG. 8. (Color online) Variations of average electron temperature, T_e, average power density, Q, [H]/[H_2] ratio and T_{gas} in the hottest central zone of the plasma region (i.e. $r=0$, z_C, where the point $r=0$, $z=0$ defines the substrate center) as functions of $X_0(H_2)$ in CH_4/H_2/Ar mixtures. The value of $X_0(CH_4)$ used in these calculations was 0.5% for the Ar-rich conditions [$X_0(H_2)=1$, 14.7 and 25%] and 4.4% for the H_2-rich conditions [$X_0(H_2)=88.6\%$]. The average power density was estimated from the relation $Q=P/V$, where V is the plasma volume and the total power P varies in the range 0.5–1.5 kW as indicated.

relevant (low energy) excited states for dissipating the electron energy in an Ar-rich plasma is much smaller. Thus the absorbance capacity of the $0.5\%CH_4/1\%H_2$/Ar plasma is limited to much lower power densities ($Q < 2$ W cm^{-3} in the core region, where H_2 is substantially dissociated [e.g., $X(H_2) \sim 0.7\%$, $X(H) \sim 1.85\%$] increasing to $Q \sim 5$ W cm^{-3} in the near substrate region, where $X(H_2) \sim 1.6\%$ and $X(H) \sim 0.16\%$). Absorption of any given P thus requires a larger volume of Ar-rich plasma than of H_2-rich plasma. Progressive replacement of H_2 by Ar in a C/H/Ar plasma operating at constant input power must therefore result in some expansion of the plasma volume, especially at high Ar dilutions [$X_0(Ar) > 85\%$] — as illustrated in Figs. 7 and 8. The present analysis allows estimation of the maximum input power (P_{max}) that can be absorbed in the $0.5\%CH_4/1\%H_2$/Ar mixture: $P \leq P_{max} = Q_{C/H/Ar} V_{reactor}$. For the purpose of this estimation, we approximate the power density as $Q_{C/H/Ar}$ [W cm^{-3}] $\approx 0.36 \times 10^{-11} \times (p/T_{gas}) \times (E/N)^2 \times n_e$ (Ref. 26) and assume a reduced electric field E/N (in units of Td $= 10^{-17}$ V cm^2) $\approx 5.5 + 0.26 \times X(H_2)$ (deduced from plasma-chemical and electron kinetics calculations for the present conditions in Ar and H_2-rich plasmas).[26,36] p in the expression for $Q_{C/H/Ar}$ is in units of Torr, and $X(H_2)$ is the local H_2 mole fraction in %. Thus we deduce $P_{max} \sim 1.1$ kW for the present MW PECVD reactor and plasma parameters, i.e., chamber volume $V_{reactor} \approx 600$ cm^3, average H_2 mole fraction $X(H_2) \sim 1\%$, average $n_e \sim 3 \times 10^{11}$ cm^{-3} and $T_{gas} \sim 3000$ K.

The variation in plasma volume with changes in H_2/Ar fraction ensures near constant maximal T_{gas} values ($T_{gas,max} \sim 2900-3100$ K) in C/H/Ar plasmas operating over a wide range of process conditions (spanning the spectrum from H_2-rich to Ar-rich) — as illustrated in Figs. 7 and 8, and in our previous studies of H_2-rich plasmas.[23] Such a finding is contrary to possible expectations based on the fact that Ar has much lower thermal conductivity (λ) than H_2 ($\lambda_{Ar} \sim 0.1\lambda_{H2}$), which might have encouraged the view that Ar-rich plasmas would support much higher gas temperatures. The only visible consequence of the different thermal conductivities and plasma volumes in the false color spatial distribution plots for C/H/Ar plasmas with differing $X_0(H_2)$ (Fig. 7) is the steeper temperature gradient near the reactor walls when operating under UNCD [$X_0(H_2) = 1\%$] conditions. Given $\lambda_{Ar} \ll \lambda_{H2}$, the steeper gradient in the case of low $X_0(H_2)$ is inevitable, given that similar powers need to be conducted from the hot gas to the cold reactor walls in both cases.

C. H/Ar plasma versus C/H/Ar plasma. Differences in the ionization/recombination balance

As noted previously, tracing the complex balance between ionization and recombination reactions involving the various charged species, and their variation with n_e and temperature under the various H/Ar and C/H/Ar plasma compositions required particular care and attention. For example, the CRDS measurements show an order of magnitude drop of {H($n = 2$)} upon stopping the CH_4 flow [Fig. 4(b)]. This drop indicates a serious perturbation of the plasma parameters, which the plasma chemistry model must explain. The main source of ions in an H_2-rich C/H/Ar plasma is electron impact ionization of the dominant hydrocarbon (C_2H_2),[26] with lesser contributions from associative ionization involving electronically excited atoms H($n > 1$), Ar*, e.g.,

$$H(n > 1) + H_2 \rightarrow H_3^+ + e, \quad (1)$$

$$H(n > 1) + Ar \rightarrow ArH^+ + e, \quad (2)$$

With increasing $X_0(Ar)$, ionization processes involving metastable ($3p^5 4s^1$) states Ar*, e.g.,

$$Ar^* + H \rightarrow ArH^+ + e, \quad (3)$$

$$Ar^* + C_2H_2 \rightarrow C_2H_2^+ + Ar + e \quad (4)$$

become increasingly important, and ionization pathway (3) becomes dominant in an Ar-rich plasma if we assume the following rate coefficients: $k_1(n) = 1.66 \times 10^{-11} \exp(-E_n/T_{gas})$ cm^3 s^{-1}, $E_2 = 8120$ K and $E_{n>2} = 0$; $k_2 = k_1/2$; $k_3 = 1.66 \times 10^{-11}$ cm^3 s^{-1} and $k_4 = 3.32 \times 10^{-11}$ cm^3 s^{-1} (Ref. 26). The most important gas-phase loss process for charged species is the dissociative recombination of electrons with the dominant $C_yH_x^+$ ions in both H_2-rich ($y = 2$, $x = 2,3$) and Ar-rich ($y = 2$, $x = 2,3$, and $y = 3$, $x = 1$) C/H/Ar plasmas,[26] i.e.,

$$C_yH_x^+ + e \rightarrow C_yH_{x-1} + H. \quad (5)$$

Stopping the CH_4 flow obviously affects the ionization/recombination balance. It removes the hydrocarbon ions, and the contribution from electron impact ionization of C_2H_2. Direct ionization of other species is unimportant in Ar-rich H/Ar plasmas, in which the associative ionizations (1)–(3) prevail. The most obvious changes are in the recombination rates when the dominant ions switch from $C_yH_x^+$ to H_3^+ and ArH^+. The recombination rates for polyatomic ions like $C_yH_x^+$ are large ($k \sim 10^{-6}$ cm^3 s^{-1}) at room temperature, and decline with T_e as $k \sim 1/T_e^a$, where $a \sim 0.6-0.8$.[37,38] Simpler ions have fewer available dissociative recombination pathways. Unfortunately, the relevant rate coefficients are not well known, especially at high electron and ion temperatures. Recent studies of Ar atom appearance rates from e−ArH^+ collisions return extremely low rate coefficients ($k < 5 \times 10^{-10}$ cm^3 s^{-1}) at the low ($T_e < 1.5$ eV) collision energies relevant to the present conditions.[39] This implies that the rate coefficient for e-ArH^+ recombination is much (~two orders of magnitude) lower than that for e−$C_yH_x^+$ recombination. For the present modeling, we assume $k_5 = 3.5 \times 10^{-8}/T_e^{0.68}$ cm^3 s^{-1} (T_e in eV), and $k_{6,7} = 4.8 \times 10^{-10}$ cm^3 s^{-1} for the recombination reactions:

$$ArH^+ + e \rightarrow Ar + H(n = 2), \quad (6)$$

$$H_3^+ + e \rightarrow H_2 + H(n = 2). \quad (7)$$

Using these recombination coefficients, the 2D model calculations show a substantial drop in the electron temperature upon cutting the CH_4 flow [from $T_e = 1.74$ eV with $X_0(CH_4) = 0.5\%$ to $T_e = 1.28$ eV for $X_0(CH_4) = 0\%$], which has the effect of lowering the ionization rate (bringing it closer to the much reduced recombination rate). However, and in contrast to the case of a C/H/Ar plasma, the

production and loss rates of charged species in an H/Ar plasma are not in local balance. Recombination reactions only compensate ~15%–20% of the associative ionization in the bulk of an H/Ar plasma. Overall balance is achieved by ambipolar diffusion of charged species to the substrate and to the periphery of the plasma, where they are neutralized. The above plasma chemical mechanism predicts a ~sevenfold drop of $\{H(n=2)\}$ at $z=9.5$ mm [Fig. 4(b)], and that the $0\%CH_4/14.7\%H_2$/Ar mixture will occupy a larger plasma volume than the base ($0.5\%CH_4/14.7\%H_2$/Ar) mixture: $V \sim 295$ cm^3 cf. ~210 cm^3.

D. Variations in reactor parameters: 2D model versus experimental results and trends

The previous plasma-chemical mechanism,[26,27] supplemented by the important reaction (3) and the reduced recombination coefficients $k_1(n=2)$, $k_2(n=2)$, k_6 and k_7, was used in a systematic 2D modeling study of the various experimental regimes. The modeling captures the many changes in plasma parameters induced by varying $X_0(H_2)$, $X_0(CH_4)$, p and/or P in C/H/Ar mixtures, reproduces much of the CRDS and OES data and the observed trends well (as illustrated in Figs. 4–6 and in Sec. III C), and allows us to trace the various complex interdependencies between plasma species and temperatures T_{gas} and T_e. The measured $C_2(a)$ rotational temperature, and the Balmer-α profiles were used as additional tests of the model results for UNCD plasma conditions. The poorest agreement between experiment and model prediction is for the pressure dependence of $\{H(n=2,3)\}$ – which may reflect an overly simplistic modeling of the resonance radiation transfer. Additionally, we note that the calculated $\{C_2(a, v=0)\}$ column densities systematically exceed the measured values in the case of Ar-rich plasmas [e.g., calculated $\{C_2(a,v=0)\}=1.57\times10^{14}$ cm^{-2}, cf. the measured value $\{C_2(a,v=0)\}=2.8\times10^{13}$ cm^{-2}]. This may well reflect the presence of additional mechanisms for C_2 conversion to higher hydrocarbon species and/or to carbon nanoparticles that become increasingly effective at high $[H]/[H_2]$ ratios (and thus high C_y concentrations) but which are not included in the present plasma-chemical mechanism.

One important effect returned by the 2D modeling is the marked rise in $[H]/[H_2]$ ratio in Ar-rich plasmas. The main source of atomic hydrogen is thermal dissociation: $H_2+M \leftrightarrow 2H+M$, with $M=H_2$, Ar. The rate of thermal dissociation exceeds the reverse recombination rate at high temperatures $T_{gas} > T_c$, where the critical temperature T_c depends on the degree of dissociation (e.g., T_c ~2700 K in a $0.5\%CH_4/14.7\%H_2$/Ar mixture, cf. T_c ~2400 K in a $4.4\%CH_4/88.6\%H_2$/Ar mixture). The maximal $[H]/[H_2]$ value calculated here for the base mixture is ~0.5 (cf. $[H]/[H_2]$ ~0.09 in a $4.4\%CH_4/88.6\%H_2/7\%$Ar mixture), notwithstanding the fact that the former plasma is activated with a lower input power ($P=1$ kW, cf., 1.5 kW). Three factors are responsible for this increase — the larger hot volume, the lower diffusion coefficient of H atoms in Ar-rich plasmas and the higher electron temperature (Fig. 8). Note that the H atom production rate from electron impact dissociation of H_2 becomes comparable to that from thermal dissociation under UNCD conditions.

These effects lead to extremely high $[H]/[H_2]$ ratios (~2.5) in the Ar dominated plasmas used for UNCD growth in a MW PECVD reactor (here modeled as $0.5\%CH_4/1\%H_2/98.5\%$Ar, $P=0.5$ kW). Under these conditions, electron impact excitation of H_2 and thermal dissociation make comparable contributions to the H atom production rate. Given such high $[H]/[H_2]$ ratios, the fast H-shifting (i.e., $CH_x+H \leftrightarrow CH_{x-1}+H_2$) reactions all favor products, with the result that atomic carbon is calculated to be the dominant CH_x species in the hot plasma region ($[C]$ ~5.9×10^{13} cm^{-3} $\gg$ $[CH]$ ~1.7×10^{12}, $[CH_2]$ ~2.9×10^{11}, $[CH_3]$ ~5.7×10^{10} cm^{-3}, and $[CH_4]$ ~1.4×10^9 cm^{-3}). A similar shift in favor of $[C_2]$ and $[C_3]$ is calculated for the C_2H_x and C_3H_x groups in the core plasma region, due to a combination of thermal decomposition (of C_yH_2 and C_yH, $y=2$, 3) and the H-shifting reactions, e.g., $C_2H_2+H \leftrightarrow C_2H+H_2$ and $C_2H+H \leftrightarrow C_2(X)+H_2$, with the result that $[C_2]_{total}$ (i.e., the sum of $[C_2(a)]$ and $[C_2(X)]$)~1.04×10^{14}, $[C_2H]$ ~1.16×10^{14}, $[C_2H_2]$ ~3×10^{14} cm^{-3}, and $[C_3]$ ~4.6×10^{14}, $[C_3H]$ ~5.4×10^{11}, $[C_3H_2]$ ~2.3×10^{12} cm^{-3}. Such distributions are very different from those found in the cores of plasmas involving higher H_2 fractions, wherein C_2H_2 will normally be the dominant carbonaceous species. Thus, for example, the present 2D modeling of our base plasma ($X_0(H_2)=14.7\%$) returns $[C_2H_2]$ ~1.1×10^{15} $\gg$ $[C_2H]$ ~8.6×10^{13}, $[C_2]_{total}$ ~1.5×10^{13}, $[C]$ ~2×10^{13}, $[CH]$ ~3.2×10^{12}, $[CH_3]$ ~2.9×10^{12} and $[C_3]$ ~2.7×10^{13} cm^{-3} in the hot plasma core. Even in the case of UNCD plasmas, the dominance of species like C, C_2, and C_3 is limited to the hot core region; the predicted concentrations of such species in the cooler regions are very much lower. The CH_3 concentration maximizes in cooler, off plasma regions (T_{gas} ~1300 K).[26] These large spatial variations in the various radical densities are illustrated in Fig. 9. Figure 9(a) shows the 2D distributions of CH_3 and $C_2(a)$ radical concentrations under the present base conditions ($X_0(H_2)=14.7\%$), while Fig. 9(b) displays the calculated C_3 and $C_2(a)$ radical concentration distributions for our model UNCD plasma. The calculated spatial distributions of CH and C radicals in the latter conditions are not shown [since they are very similar to that calculated for $C_2(a)$ radicals], while the CH_3 radical density in the UNCD plasma shows a barrel-like spatial distribution similar to that calculated for the present base conditions [Fig. 9(a)]. The C_3 distribution shown in Fig. 9(b) underpins the "explosion" of C_3 emission observed under UNCD plasma conditions [Fig. 6(a)].

The large variations in the various species concentrations with T_{gas} and with $[H]/[H_2]$ ratio are even more obvious from Table I, which shows $[CH_3]$ ~1.5×10^{12} cm^{-3}, $[C]$ ~7.5×10^{10} cm^{-3} and $[C_2]_{total}$ ~1.2×10^{10} cm^{-3} for the UNCD plasma conditions at $r=0$, $z=0.5$ mm, i.e., just above the center of the substrate. The fact that the calculated [C] at $z=0.5$ mm is only one order of magnitude lower than $[CH_3]$, allied to the lower T_{sub} (see later), might be seen as encouraging the recent suggestion that insertion of gas phase C atoms into surface CH bonds could be a contributory mechanism for UNCD growth;[40] indeed, this density at the growing surface, coupled with an assumption that the insertion reaction occurs with unit probability, could provide the UNCD growth rates observed experimentally (e.g., G ~0.1 μm h^{-1} at $T_{sub}=873$

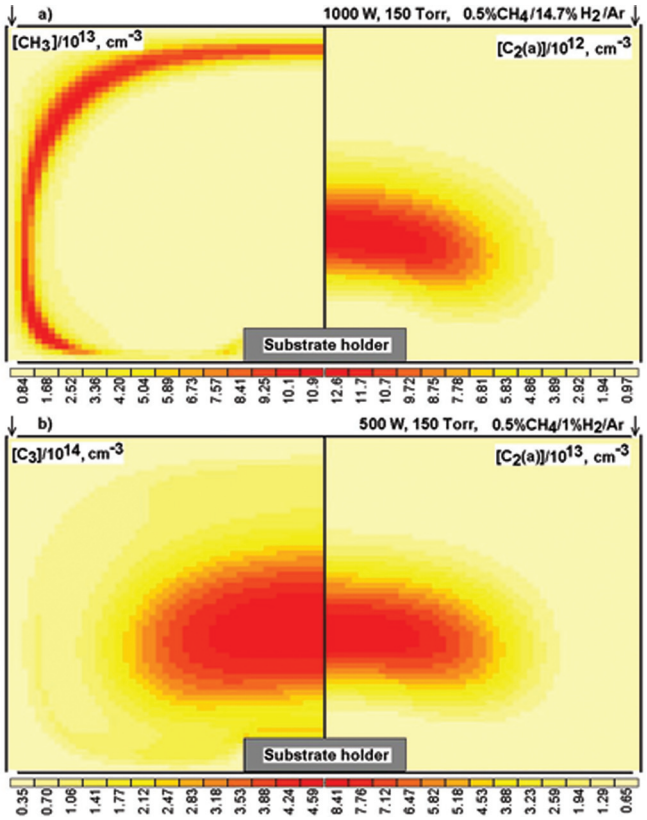

FIG. 9. (Color online) 2D(r, z) model distributions of: (a) CH_3 (left) and CH (right) number densities for the present base conditions and (b) C_3 (left) and $C_2(a)$ (right) number densities for the UNCD growth conditions (0.5%CH_4/1%H_2/98.5%Ar, $p = 150$ Torr, $P = 0.5$ kW). Again, the vertical (z) and radial (R_r) dimension of the simulated reactor is 6 cm.

K).[41,42] However, the temperature dependencies of the equilibria linking the various CH_x species will ensure [and additional calculations with a finer grid size ($d_z = 0.25$ mm, cf. $d_z = 1$ mm) confirms] further processing away from C and toward CH_3 and larger species in the near substrate region $0 \leq z \leq 0.5$ mm, and a number of alternative proposals have appeared. For example, several analyses now favor CH_3 as the probable UNCD growth species.[27,42] The marked increase in CH_3 concentrations in the near substrate boundary layer [such a boundary is clearly evident at the periphery of the hot region in Fig. 9(a)] could provide [CH_3 ($z = 0$)] $\sim 10^{13}$ cm^{-3} and consequent UNCD growth rates G $\sim 0.05-0.1$ μm h^{-1}.[27,42] Recent mass-spectrometric studies of the relative densities of different C_yH_x species in C/H/Ar plasmas and their variation with Ar dilution have led to a suggestion that all CH_x, $x = 0-3$ species could contribute to UNCD growth.[43] This work also finds an anti-correlation between UNCD growth rates and the measured C_2 radical densities. Further careful investigation of species distributions in the (nonthermally equilibrated) boundary layer just above the substrate surface, and of possible conversions of C_yH_x ($y = 1-3$) species to higher carbons, hydrocarbons and, possibly, nanoparticles would clearly be beneficial. Preliminary additional calculations including just the $C_3 + C_3 \leftrightarrow C_6$ reaction[44,45] suggest C_6 radical concentrations comparable with [C_3] in the low temperature ($T_{gas} < 1500$ K) regions, e.g., in the near substrate region.

E. Power balance and heat loss to the substrate, reactor walls and the quartz window

The 2D modeling also allows investigation of the various dissipation pathways for MW power absorbed in the reactor, and comparison between the calculated weights of these pathways relative to measured rises in the temperature of the cooling water. The main power dissipation pathways revealed by the 2D modeling are (i) thermal conduction fluxes, from the hot plasma to the reactor walls, baseplate and top plate (window), (ii) radiation losses and (iii) substrate heating — both from the thermal conduction flux and from the incident flux of atomic H. Notwithstanding the very high [H]/[H_2] ratio (~ 2.5) in the core of the hot UNCD plasma [$X_0(H_2) = 1\%$], the actual H atom concentration in these plasmas is $\sim 3.7\times$ lower than that in the core of the base plasma [$X_0(H_2) = 14.7\%$, $P = 1$ kW]. The lower [H] must result in reduced substrate heating[46] from H atom adsorption at the C* surface radical sites.[47] Another, more important, reason for the observed drop in T_{sub} when operating with UNCD plasma conditions [T_{sub} ~ 785 K, cf. ~ 1130 K for the present base conditions, with $P = 1.0$ kW in both cases (Fig. 2)] is the much reduced thermal conductivity of the Ar dominated plasma, and thus of the conductive heat flux to the substrate. The calculated contributions to substrate heating from heat conduction and from H atom adsorption on C* surface sites are, respectively: 27 and 3.4 W for UNCD conditions [$X_0(H_2) = 1\%$, $P = 0.5$ kW), 57.4 and 22 W for the present base conditions ($X_0(H_2) = 14.7\%$, $P = 1$ kW], 80 and 28 W for $X_0(H_2) = 25\%$, $P = 1$ kW, and 277 and 41.6 W for the H_2-rich conditions (4.4%CH_4/7% Ar/H_2, $P = 1.5$ kW),[23] under which conditions the power loading to the substrate reaches ~45 W cm^{-2}.

Thus we see that the flux of atomic H is only responsible for $\sim 12\%-30\%$ of the total substrate heating, and that the total substrate heating increases almost linearly, by a factor ~ 10 on changing from Ar-rich to H_2-rich plasma conditions (albeit with changes in P also). T_{sub} is determined by the balance of the heat loading and the gas cooling system. The much higher ($\sim$10-fold) substrate heating rate in the H_2-rich plasma is compensated by enhanced heat abstraction from the H_2-rich gas due to the higher (again $\sim$10-fold) thermal conductivity of H_2 gas as compared with Ar. The local maximum of T_{sub} is found at $X_0(H_2) = 20\%$, at which ratio Ar and H_2 make comparable contributions to the total conductivity.

The plots of power balance versus $X_0(H_2)$ shown in Fig. 2 merit careful consideration. The experimentally measured temperature rise, dT_{water}, of the cooling water flowing through the reactor side walls and the baseplate (including the substrate and substrate holder) provide valuable insights into the operation of the MW reactor and the plasma parameters. First, we can calculate the power P_{water} carried away by the water flow $F(H_2O)$ using the measured dT_{water} values and the specific heat capacity of water ($C = 4187$ J kg^{-1} K^{-1}): P_{water} [W] $= a \times C \times \mathrm{d}T_{water} \times F(H_2O)$[kg min^{-1}]/60 $\approx a \times 70 \times \mathrm{d}T_{water} \times F(H_2O)$. The experimental data displayed in Fig. 2(b), obtained using $F(H_2O) = 1$ kg min^{-1}, has been plotted using a scaling factor $a = 2$ so as to raise the sum of

TABLE I. Calculated concentrations (in cm^{-3}) of selected species at $z=0.5$ mm above the substrate center in 0.5%CH_4/1%H_2/Ar, 0.5%CH_4/14.7%H_2/Ar, 0.5%CH_4/25%H_2/Ar and 4.4%CH_4/88.6%H_2/7%Ar gas mixtures, at $p=150$ Torr, $P=0.5$, 1, 1 and 1.5 kW, respectively, and the appropriate (experimentally determined) T_{sub} in each case. The last two columns illustrate the variations induced by changing the power (0.6 kW) and pressure (225 Torr) away from the present base values. The calculated gas temperatures, fraction of surface radical sites $C_s*/(C_s*+C_s–H)$ and H atom concentrations H_s just above the substrate ($z=0$, calculated as reported in Ref. 41) are presented also.

	0.5%CH_4/x%H_2/balance Ar					
Mixture	$x=1\%$	$x=14.7\%$	$x=25\%$	4.4%CH_4/88.6%H_2/Ar	0.5%CH_4/14.7%H_2/Ar	0.5%CH_4/14.7%H_2/Ar
P/kW	0.5	1.0	1.0	1.5	0.6	1.0
p/Torr	150	150	150	150	150	225
T_{sub}/K	750	1130	1200	973	1130	1130
H	1.99×10^{15}	5.40×10^{15}	5.02×10^{15}	8.14×10^{15}	3.84×10^{15}	8.44×10^{15}
H_2	2.10×10^{16}	1.63×10^{17}	2.79×10^{17}	1.04×10^{18}	1.79×10^{17}	2.41×10^{17}
CH_4	9.92×10^{12}	4.42×10^{12}	1.08×10^{13}	9.56×10^{14}	7.32×10^{12}	1.21×10^{13}
CH_3	1.51×10^{12}	1.79×10^{12}	3.21×10^{12}	1.08×10^{14}	2.41×10^{12}	4.59×10^{12}
CH_2	4.61×10^{9}	2.39×10^{10}	3.86×10^{10}	4.56×10^{11}	2.77×10^{10}	6.65×10^{10}
$CH_2(s)$	1.32×10^{8}	7.65×10^{8}	1.14×10^{9}	1.13×10^{10}	8.10×10^{8}	2.35×10^{9}
CH	1.29×10^{9}	3.23×10^{9}	3.09×10^{9}	1.70×10^{10}	2.61×10^{9}	9.80×10^{9}
C	7.48×10^{10}	6.89×10^{10}	3.92×10^{10}	4.87×10^{10}	3.20×10^{10}	1.86×10^{11}
C_2H_2	2.43×10^{15}	2.43×10^{15}	2.46×10^{15}	1.04×10^{16}	2.63×10^{15}	3.40×10^{15}
C_2H	3.00×10^{11}	4.55×10^{10}	3.93×10^{10}	3.30×10^{10}	3.87×10^{10}	8.36×10^{10}
$C_2(a)$	8.82×10^{9}	2.36×10^{8}	1.02×10^{8}	1.68×10^{8}	1.59×10^{8}	4.40×10^{8}
$C_2(X)$	3.37×10^{9}	5.62×10^{7}	2.61×10^{7}	1.56×10^{7}	3.29×10^{7}	1.19×10^{8}
C_3	1.83×10^{14}	1.83×10^{13}	4.95×10^{12}	1.15×10^{13}	8.35×10^{12}	3.47×10^{13}
C_3H	1.31×10^{12}	1.03×10^{11}	4.35×10^{10}	1.73×10^{11}	5.95×10^{10}	2.25×10^{11}
C_3H_2	1.43×10^{14}	2.83×10^{13}	2.05×10^{13}	1.93×10^{14}	2.37×10^{13}	5.51×10^{13}
C_4H_2	1.47×10^{14}	3.30×10^{12}	1.95×10^{12}	1.74×10^{13}	3.57×10^{12}	4.71×10^{13}
T_{gas}/K	1086	1365	1422	1314	1379	1391
$C_s*/(C_s*+C_s–H)$	0.033	0.125	0.131	0.083	0.12	0.122
H_s	4.00×10^{14}	5.37×10^{14}	6.33×10^{14}	1.82×10^{15}	4.23×10^{14}	6.36×10^{14}

the measured powers close to the total input power $P=1$ kW and the 2D model predictions. The origin of the scaling factor a is not clear. The calorimetric procedure employed may underestimate the dissipated power. Alternatively, the difference may reflect additional, unmonitored power dissipation pathways through the solid parts of reactor. The 2D model results included in Fig. 2(b) have also been scaled — by a factor of 1/P[kW] (i.e., by a factor of 2 for the model UNCD plasma conditions, by 2/3 for the plasma with $X_0(H_2)=88.6\%$ and by 1 for the remaining modeled plasma conditions) — in order to facilitate comparison with the experimental power dissipation data all of which was measured at $P=1$ kW. Note that the different power dissipation pathways are only approximately proportional to the total power (P_{total}), and that the calculated powers used in substrate heating are included, as in the experiment, in the baseplate heating term. As Fig. 2 showed, decreasing $X_0(H_2)$ results in a progressive increase in the fraction of P_{total} expended in wall heating and a decrease in the fraction dissipated through baseplate heating — consistent with the observation that the hot plasma volume expands, and rises slightly from the baseplate (and substrate) as H_2 is progressively replaced by Ar.

The second important effect evident from Fig. 2 is the drop in the total power abstracted via the cooling water (i.e., the sum of the two experimental curves) in the case of the UNCD plasma. We can envisage two contributory reasons for the implied power shortfall — an increase in the unmonitored power lost via heating of the top quartz window, and/or radiation losses. As discussed previously, the precise location of the plasma is sensitive to the process gas mixture, but the 2D model calculations show no marked increase in the conduction flux to the quartz under UNCD conditions. What the calculations do reveal, however, is a sharp increase in the density of excited carbon radical species [mainly C_3* in the present modeling — recall Figs. 4(a), 6(a), and 9(b)] under UNCD plasma conditions, which will result in a significant radiative power loss even when, as in the present modeling, only three singlet excited states of C_3 [the $A^1\Pi_u$ (term value ~3.85 eV), $A^1\Pi_g$ (~4.56 eV) and $^1\Sigma_u^+$ (~8.1 eV) states][48,49] are considered. The calculated rate coefficients for electron impact excitation from the $X^1\Sigma_g^+$ ground state to these states are quite large (e.g., k[e-$C_3(X^1\Sigma_g^+)$] $=8.4\times10^{-9}$, 4.3×10^{-9} and 3.8×10^{-10} cm^3 s^{-1}, respectively, at $T_e=2.5$ eV, comparable to that for exciting the $C_2(d^3\Pi_g\leftarrow a^3\Pi_u)$ Swan system at 516.5 nm $\{k$[e-$C_2(a)$], $T_e=2.5$ eV$\}=4.1\times10^{-9}$ cm^3 s^{-1} calculated using cross-sections from Ref. 50) and sufficient to account for radiation loss up to ~30% of the total input power under UNCD plasma conditions. Emitted photons with energies $\epsilon>5$ eV will be absorbed in the quartz window, providing an additional heating term (e.g., ~8 W calculated for just the $C_3(^1\Sigma_u^+\rightarrow X^1\Sigma_g^+)$ emission, amounting to ~12% of the total quartz heating) that is clearly evident under UNCD plasma conditions in Fig. 2. The enhanced heating of the quartz window is also discernible

experimentally, through temperature measurements of the air flow used to cool the upper surface of this window.[51]

V. CONCLUSIONS

We have extended our previous experimental/modeling studies of H_2-rich C/H/Ar plasmas (e.g. 4.4%CH_4/88.6%H_2/7%Ar, $F_{total} = 565$ sccm, $p = 150$ Torr, $P = 1.5$ kW) such as are used for growth of MCD films[22–25] to explore the consequences of major variations in the input H_2/Ar ratio — from H_2/Ar mole fraction ratios of $> 10:1$ as used for MCD growth, through ratios $\sim$1:6 (e.g., 0.5%CH_4/14.7%H_2/84.8%Ar, $F_{total} = 525$ sccm, $p = 150$ Torr, $P = 1.0$ kW, the "base" conditions used in most of the present work) typical of those used for NCD growth, and extending to an H_2/Ar ratio of $\sim$1:99 (e.g., 0.5%CH_4/1%H_2/98.5%Ar, $F_{total} = 525$ sccm, $p = 150$ Torr, $P = 0.5$ kW) as used for growth of UNCD material. As before, absolute column densities of $C_2(a)$ and CH(X) radicals and of H($n = 2$) atoms have been determined by CRDS, as functions of z and of process conditions [$X_0(H_2)$, $X_0(CH_4)$, X_0(Ar), p, and P]. OES methods have also been used to explore the relative densities of electronically excited H atoms, and CH, C_2, and C_3 radicals, as functions of these same process conditions. Measurements of the temperature rise in the water flow cooling the reactor walls and base have allowed some insights into the ways in which the input MW power is dissipated, and how this varies with the H_2/Ar ratio in the source gas mixture.

The experimental studies have again been complemented by extensive 2D(r, z) modeling of the plasma chemistry, composition and parameters, which offers a quantitative rationale for most of the present observations. Substituting H_2 by Ar (at constant p and P) results in substantial expansion of the plasma volume. In the case of standard MCD (H_2-rich) plasmas, $> 90\%$ of the input MW power is absorbed through rovibrational excitation of H_2. Reducing the H_2 content (as in an NCD or, particularly, a UNCD plasma) necessarily reduces the absorbed power densities; the Ar-rich plasma thus expands to accommodate a given input power. The average power density in the core of a UNCD plasma is an order of magnitude less than that in a representative MCD plasma. Progressive replacement of H_2 by Ar leads to increases in the electron temperature and electron density within the plasma, a reduction in [H] but an increase in [H]/[H_2] ratio, and little change in the maximum T_{gas} (which is consistently $\sim$3000 K) — notwithstanding the lower thermal conductivity of Ar ($\lambda_{Ar} \sim 0.1\lambda_{H2}$) which might have encouraged the view that Ar-rich plasmas would support significantly higher T_{gas} values. The CH(X) and $C_2(a)$ radical column densities measured for the present base conditions are, respectively, $\sim$4 and $\sim$10 times greater than those reported for the standard MCD plasma,[23] despite the fact that $X_0(CH_4)$ used in the present studies is $\sim$nine times smaller than that used in the earlier study. These differences can be traced to the increased [H]/[H_2] ratio at higher X_0(Ar), which pushes the fast H-shifting ($C_yH_x + H \leftrightarrow C_yH_{x-1} + H_2$; $y = 1-3$) equilibria to the right —thereby favoring "product" species like C atoms, C_2, and C_3 radicals. The optical emission from Ar-rich C/H/Ar plasmas is increasingly dominated by excited state C_2 and C_3 radicals, and radiative power losses start to become comparable with other power dissipation pathways (e.g., heat conduction to the reactor walls and the reactor base) in UNCD plasmas. The present study also confirms previous suggestions[27,42] that reported UNCD growth rates ($G \sim 0.05-0.1$ μm h^{-1}) can be accommodated by the calculated concentrations of CH_x radicals (i.e., CH_3 radicals), though the detailed mechanism of UNCD growth certainly merits further study.

ACKNOWLEDGMENTS

The Bristol group is grateful to EPSRC for funding (grant Nos. EP/D074924, EP/E018297), to Element Six Ltd. for financial support and the long term loan of the MW reactor, and to colleagues K. N. Rosser, Drs. J. A. Smith and C. M. Western, and Professors A. J. Orr-Ewing and P. W. May for their many contributions to the work described here. YuAM is pleased to acknowledge support from RF government for Key Science Schools grant No. 3322.2010.2. The Bristol-Moscow collaboration benefitted greatly from the award of a Royal Society Joint Project Grant.

[1] D. G. Goodwin and J. E. Butler, in *Handbook of Industrial Diamonds and Diamond Films*, edited by M. A. Prelas, G. Popovici, and L. K. Bigelow (Marcel Dekker, New York, 1998), pp. 527–581, and references therein.
[2] J. E. Butler, Yu. A. Mankelevich, A. Cheesman, J. Ma, and M. N. R. Ashfold, J. Phys. Condens. Matter **21**, 364201 (2009), and references therein.
[3] K. Hassouni, F. Silva, and A. Gicquel, J. Phys. D, Appl. Phys. **43**, 153001 (2010), and references therein.
[4] W. Zhu, A. Inspektor, A. R. Badzian, T. McKenna, and R. Messier, J. Appl. Phys. **68**, 1489 (1990).
[5] D. Zhou, T. G. McCauley, L. C. Qin, A. R. Krauss, and D. M. Gruen, J. Appl. Phys. **83**, 540 (1998).
[6] D. Zhou, D. M. Gruen, L. C. Qin, T. G. McCauley, and A. R. Krauss, J. Appl. Phys. **84**, 1981 (1998).
[7] P. Tosi, D. Bassi, B. Brunetti, and F. Vecchiocattivi, Int. J. Mass Spectrom. Ion Process. **149/150**, 345 (1995).
[8] J. Griffin and P. C. Ray, Nanotechnology **17**, 1225 (2006).
[9] H. Y. Zhou, J. Watanabe, M. Miyake, A. Ogino, M. Nagatsu, and R. J. Zhan, Diam. Relat. Mater. **16**, 675 (2007).
[10] A. Gicquel, K. Hassouni, S. Farhat, Y. Breton, C. D. Scott, M. Lefebvre, and M. Pealat, Diam. Relat. Mater. **3**, 581 (1994).
[11] A. Gicquel, M. Chenevier, K. Hassouni, A. Tserepi, and M. Dubus, J. Appl. Phys. **83**, 7504 (1998).
[12] P. W. May, Philos. Trans. R. Soc. London Ser. A **358**, 473 (2000).
[13] J. Birrell, J. E. Gerbi, O. Auciello, J. M. Gibson, J. Johnson, and J. A. Carlisle, Diam. Rel. Mater. **14**, 86 (2005).
[14] D. M. Gruen, Annu. Rev. Mater. Sci. **29**, 211 (1999).
[15] D. M. Gruen, O. A. Shenderova, and A. Ya. Vul', eds., *Synthesis, Properties and Applications of Ultrananocrystalline Diamond*, NATO Science Series Part II, Vol. 192 (Springer, New York, 2005).
[16] O. A. Williams, M. Nesladek, M. Daenen, S. Michaelson, A. Hoffman, E. Osawa, K. Haenen, and R. B. Jackman, Diam. Relat. Mater. **17**, 1080 (2008).
[17] A. V. Sumant, O. Auciello, R. W. Carpick, S. Srinivasan, and J. E. Butler, MRS Bull. **35**, 281 (2010).
[18] S. Michaelson, A. Stacey, J. Orwa, A. Cimmino, S. Prawer, B. C. C. Cowie, O. A. Williams, D. M. Gruen, and A. Hoffman, J. Appl. Phys. **107**, 093521 (2010).
[19] M. D. Wheeler, S. M. Newman, A. J. Orr-Ewing, and M. N. R. Ashfold, J. Chem. Soc., Faraday Trans. **94**, 337 (1998).
[20] J. Ma, M. N. R. Ashfold, and Yu, A. Mankelevich, J. Appl. Phys. **105**, 043302 (2009).
[21] C. J. Rennick, J. Ma, J. J. Henney, J. B. Wills, M. N. R. Ashfold, A. J. Orr-Ewing, and Yu, A. Mankelevich, J. Appl. Phys. **102**, 063309 (2007).
[22] Yu. A. Mankelevich, M. N. R. Ashfold, and A. J. Orr-Ewing, J. Appl. Phys. **102**, 063310 (2007).

[23]J. Ma, J. C. Richley, M. N. R. Ashfold, and Yu, A. Mankelevich, J. Appl. Phys. **104**, 103305 (2008).
[24]J. Ma, J. C. Richley, D. R. W. Davies, A. Cheesman, M. N. R. Ashfold, and Yu, A. Mankelevich, J. Phys. Chem. A **114**, 2447 (2010).
[25]J. Ma, J. C. Richley, D. R. W. Davies, M. N. R. Ashfold, and Yu, A. Mankelevich, J. Phys. Chem. A **114**, 10076 (2010).
[26]Yu, A. Mankelevich, M. N. R. Ashfold, and J. Ma, J. Appl. Phys. **104**, 113304 (2008).
[27]O. J. L. Fox, J. Ma, P.W. May, M. N. R. Ashfold, and Yu, A. Mankelevich, Diam. Relat. Mater. **18**, 750 (2009).
[28]F. Mohasseb, K. Hassouni, F. Bénédic, G. Lombardi, and A. Gicquel, in *Synthesis, Properties and Applications of Ultrananocrystalline Diamond*, edited by D. M. Gruen *et al*. (Springer, New York, 2005), pp. 93–108.
[29]F. J. Gordillo-Vazquez and J. M. Albella, Plasma Sources Sci. Technol. **11**, 498 (2002).
[30]C. M. Western, PGOPHER, a Program for Simulating Rotational Structure, University of Bristol, http://pgopher.chm.bris.ac.uk.
[31]G. M. Lloyd and P. Ewart, J. Chem. Phys. **110**, 385 (1999).
[32]A. N. Goyette, J. E. Lawler, L. W. Anderson, D. M. Gruen, T. G. McCauley, D. Zhou, and A. R. Krauss, J. Phys. D, Appl. Phys. **31**, 1975 (1998).
[33]J. R. Rabeau, P. John, J. I. B. Wilson, and Y. Fan, J. Appl. Phys. **96**, 6724 (2004).
[34]G. Lombardi, K. Hassouni, F. Bénédic, F. Mohasseb, J. Röpcke, and A. Gicquel, J. Appl. Phys. **96**, 6739 (2004).
[35]K. Hassouni, T. A. Grotjohn, and A. Gicquel, J. Appl. Phys. **86**, 134 (1999).
[36]Yu, A. Mankelevich, A. T. Rakhimov, N. V. Suetin, and V. Kostiuk, Diam. Relat. Mater. **5** 964 (1996).
[37]A. A. Viggiano, A. Ehlerding, S. T Arnold, and M. Larsson, J. Phys.: Conf. Ser. **4** 191 (2005).
[38]P. M. Mul and J. W. McGowan, Astrophys. J. **237**, 749 (1980).
[39]J. B. A. Mitchell, O. Novotny, J. L. LeGarrec, A. Florescu-Mitchell, C. Rebrion-Rowe, A. V. Stolyarov, M. S. Child, A. Svendsen, M. A. El Ghazaly, and L. H. Andersen. J. Phys. B **38**, L175 (2005).
[40]J. C. Richley, J. N. Harvey, and M. N. R. Ashfold, J. Phys. Chem. A **113**, 11416 (2009).
[41]P. W. May and Yu, A. Mankelevich, J. Phys. Chem. C **112**, 12432 (2008).
[42]P. W. May, J. N. Harvey, N. L. Allan, J. C. Richley, and Yu, A. Mankelevich, J. Appl. Phys. **108**, 114909 (2010).
[43]P. Csikvari, A. Somogyi, M. Veres, Gy. Hárs, and A. Tóth, Diam. Relat. Mater. **18**, 1459 (2009).
[44]R. F. Curl, Philos. Trans. R. Soc. London Ser. A **343**, 19 (1993).
[45]A. V. Terentyev, Ph.D. dissertation, TU Chemnitz, 2005.
[46]W. A. Yarbrough, K. Tankala, M. Mecray, and T. DebRoy, Appl. Phys. Lett. **60**, 2068 (1992).
[47]P. W. May, J. N. Harvey, J. A. Smith, and Yu. A. Mankelevich, J. Appl. Phys. **99**, 104907 (2006).
[48]H. Munjal and K. L. Baluja, J. Phys. B**39**, 3185 (2006).
[49]A. Terentyev, R. Scholz, M. Schreiber, and G. Seifert, J. Chem. Phys. **121**, 5767 (2004).
[50]G. Halmova, J. D. Gorfinkiel, and J. Tennyson, J. Phys. B, **39** 2849 (2006).
[51]Jie Ma, Ph.D. dissertation, University of Bristol, 2008.